Intraoperative Tissue Young's Modulus Identification During Needle Insertion Using a Laterally Actuated Needle

Thomas Lehmann, Carlos Rossa, Nawaid Usmani, Ronald Sloboda and Mahdi Tavakoli

Abstract—Needle insertion is a common minimally invasive medical procedure used for therapy and diagnosis. Among the therapeutic procedures is prostate brachytherapy, during which needle insertion is applied to implant radioactive seeds within the prostate. During insertion, the needle tends to deflect from a desired straight path thus causing misplacement of the seeds. While currently the needle is steered manually to correct for needle deflection, robotic assistance can be used towards this goal. A requirement for accurate robotic needle steering is needle deflection estimation or prediction obtained from needle deflection modeling. Various mechanics-based deflection models based on needle-tissue interactions have been introduced in the literature. Many models require the tissue Young's modulus as parameter input that can be measured or quantified using methods of varying limitations with regard to complexity or access in the operating room. This work proposes an intraoperative method for the identification of tissue Young's modulus using lateral actuation of the needle. The needle-tissue system's response in terms of needle deflection and thus tissue displacement is observed during lateral needle displacement. The tissue Young's modulus is then identified based on the energy stored in the needle-tissue system. Using this method, the actuated needle itself is the tool used to obtain the tissue Young's modulus, facilitating clinical implementation. Experimental studies are presented to confirm a high accuracy of the identified tissue Young's modulus when compared to an independent measurement. Moreover, the prediction accuracy of a deflection model that is calibrated with the proposed method is verified experimentally.
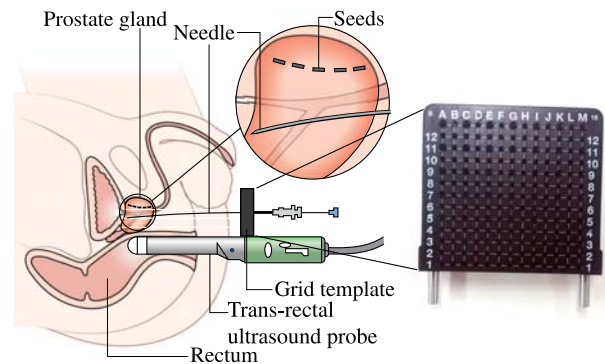
Fig. 1. A schematic representation of the radiation therapy procedure prostate brachytherapy. Radioactive seeds are implanted into the prostate with a needle guided by a grid template. The needle tip location is observed with a trans-rectal ultrasound (TRUS) probe.
(source: Cancer Research UK / Wikimedia Commons)

I. INTRODUCTION

Needle insertion is a minimally invasive medical procedure during which hypodermic needles are inserted into various regions of the body for purposes such as drug or radiation delivery, biopsy, or ablation. One procedure is prostate brachytherapy, where rice-grain-sized radioactive seeds are planted in and around the prostate tumor through hollow needles in order to eradicate cancerous tissue. A schematic representation of the procedure is shown in Fig. 1. A 5 mm fixed grid template guides the needles as they enter the patient's body. The seeds are expected to be deposited at defined locations based on a pre-determined dosage plan.

Correspondence: Thomas Lehmann, Department of Electrical and Computer Engineering, 11-203 Donadeo Innovation Centre for Engineering, 9211-116 Street NW, Edmonton, AB, Canada, T6G 1H9, Email: lehmann@ualberta.ca.

Thomas Lehmann (Corresponding Author) and Mahdi Tavakoli are with the Department of Electrical and Computer Engineering, University of Alberta, AB, Canada T6G 1H9. e-mail: {lehmann, mahdi.tavakoli}@ualberta.ca

Carlos Rossa is with the Faculty of Engineering and Applied Science, University of Ontario Institute of Technology, Oshawa, ON L1H 7K4, Canada. e-mail: carlos.rossa@uoit.ca

Nawaid Usmani is with the Department of Oncology, Cross Cancer Institute, 11560 University Avenue, Edmonton, AB, Canada, T6G 1Z2. e-mail: nawaid.usmani@albertahealthservices.ca

Ronald Sloboda is with the Division of Medical Physics, Department of Oncology, Cross Cancer Institute, 11560 University Avenue, Edmonton, AB, Canada T6G 1Z2. e-mail: ron.sloboda@albertahealthservices.ca.

During the planning phase, the needle is assumed to travel on a straight trajectory as it is inserted. As the tip of a standard brachytherapy needle is beveled, it deflects from the desired straight trajectory, which in turn leads to deviation from the desired seed locations leading to undesired and inefficient distribution of radiation. In order to minimize the amount of needle deflection, the Radiation Oncologist may execute intermittent axial needle rotations of 180° during insertion. This action rotates the beveled needle tip, which reverses the direction of needle deflection and steers the needle back towards the straight trajectory.

Robot-assisted needle steering using axial needle rotation has been the focus of significant research in the past decade with the goal of automating needle steering. Development of robotic assistant systems for needle steering demands modeling of needle-tissue interaction to estimate or predict needle deflection, image-based (e.g., ultrasound-based) measurement of needle deflection in real-time, and control algorithms for needle insertion and steering that use the aforementioned model estimates, predictions and measurement to take informed decisions for accurate needle steering towards a pre-defined target.

Many contributions in mechanics-based modeling of needle-tissue interaction or modeling of needle deflection investigate the needle-tissue contact forces occurring during insertion [1]–[13]. Other methods to model needle deflection use kinematics-based approaches such as bicycle or unicycle models [13]–[19]. The model parameters (e.g., the radius of curvature or steering angle), however, are not related to physical tissue parameters such as the tissue's Young's modulus. Thus, these models do not make use of physically meaningful and measurable quantities that can be measured

through independent tests such as tissue palpation or elastography, which is limiting. As a solution, systems that adopt kinematics-based models make use of ultrasound-image-based deflection measurements for fitting of the model parameters before the actual procedure starts [17], [20]. Multiple literature reviews that cover various subject areas of robotic needle steering are available. Misra *et al.* provide a comprehensive literature review on the modeling of needle-tissue interactions for surgical simulator applications [21]. Rossa and Tavakoli review the most recent advances in closed-loop needle steering including modeling needle-tissue interaction, needle deflection sensing, trajectory control, and hardware implementation in their literature review [22].

In the following, the most relevant works for this paper on mechanics-based needle-tissue modeling and related subjects are detailed. Mechanics-based deflection models rely on modeling of the interactions occurring between the needle and tissue such as tissue compression along the needle shaft, and various cutting-related loads at the needle tip. A detailed study considering macroscopic and microscopic needle-tissue interactions was proposed by Misra *et al.* [5]. Their model includes tissue elasticity and rupture toughness, and accordingly accounts for the needle tip and shaft interactions as the needle cuts through tissue. The model is based on the energy stored in the bent needle and tissue, and work done by the various loads acting on the needle during insertion. Roesthuis *et al.* further developed Misra *et al.*'s modeling approach to incorporate friction between needle and tissue and account for multiple axial needle rotations [6], [8]. Khadem *et al.* developed a comprehensive dynamic model for needle deflection that incorporates insertion velocity to be used as a further control input along with axial needle rotation [9]. Khadem *et al.* also developed a two-body rigid/flexible dynamic model that allows for a wider variety of control commands such as insertion velocity, axial rotation, and needle base force/torque to be used for real-time needle steering control [13]. Rossa *et al.* modeled the tissue compression along the needle shaft as virtual springs [11] in their quasi-static deflection model. To determine the amount of tissue compression at a given position along the needle, the difference between the needle shaft's deflection shape and the tip trajectory is considered accounting for an arbitrary amount of axial needle rotations. Most of the above-mentioned mechanics-based (physical) models for needle deflection require the tissue's Young's modulus to model tissue compression occurring due to the deflecting needle shaft during insertion.

Common methods to quantify the Young's modulus of biological tissue are palpation [23], [24], or compression tests, and ultrasound elastography (e.g., shear wave measurement based on the ARFI imaging technique) [20], [25], [26]. While these methods are capable of accurately quantifying tissue Young's modulus, they are not always or widely available during or even prior to a prostate brachytherapy intervention.

As stated above, multiple needle deflection models take tissue Young's modulus as a parameter, which can be difficult to obtain in a clinical setting prior to or during the surgical procedure due to a lack of equipment, limited access, or interference with standard surgical routines for each procedure.

Some of past research proposes that initially one or multiple insertions are done without needle steering in order to obtain needle deflection measurements that can then be used to identify the tissue Young's modulus, enabling model-based steering of the needles in future insertions [12], [17].

This work proposes a novel method for identifying tissue Young's modulus using a needle that is being inserted into tissue, provided the needle can also be laterally displaced outside of tissue by, for example an actuated needle guide. A schematic representation of the needle with lateral displacement applied by the actuated guide is shown in Fig. 2. The needle, which is fixed in terms of lateral motion and rotation by a fixed needle guide (i.e., the fixed guide template, see Fig. 1), is inserted into tissue up to a depth d_K and then laterally displaced by the actuated needle guide. The resulting deflection causes the tissue surrounding the needle to be deformed. The mechanical work of the actuated guide and the needle shape can be measured using a force/torque sensor and an ultrasound (US) probe, respectively. The needle-tissue system is governed by the conservation of energy principle, which states that the work applied to a system must equal its potential energy in steady state. With the force applied by the actuated guide to the needle-tissue system (F_l) and the needle deflection shape known, the tissue Young's modulus K can be determined. The identified tissue Young's modulus can then be used in mechanics-based needle deflection models.

Our approach provides a direct method for Young's modulus identification as the needle itself is the tool used to displace the tissue and measure the response. The method can be used intraoperatively where the needle insertion will only need to be paused briefly at a shallow depth to obtain the tissue Young's modulus, meaning that there will not be much interference with the current prostate brachytherapy procedure. Therefore, the method does not increase the needle insertion time or degree of invasiveness noticeably. It should be noted that the apparatus for applying lateral needle displacement can be also used for more accurate needle steering. Thus, the presented method for Young's modulus identification is an important step towards the development of an assistant system that is able to steer the needle in an integrated and intelligent manner.

Lastly, as we have shown before [12], the availability of the tissue Young's modulus can facilitate non-image-based needle deflection prediction and steering in the sense that the US transducer can be used by the surgeon for visualization and monitoring purposes and does not have to be tied to the robotic system for the entire procedure. In this work, we revisit the prior work on deflection modeling and prediction by Rossa *et al.* [12] and incorporate the method for Young's modulus identification proposed in this work into prediction of needle deflection. The objective is to show the feasibility of the integrated Young's modulus identification method with regards to clinical implementation in robot-assisted needle insertion.

The remaining sections of this paper are organized as follows. The proposed method for tissue Young's modulus identification is presented in Section II. In Section III, the integration of the method with model-based prediction of needle deflection is presented. The experimental validation of the method follows in Section IV-C. An experimental assessment
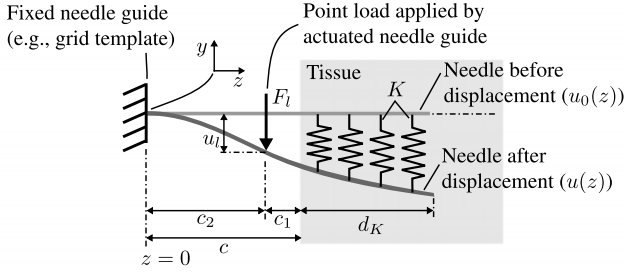
Fig. 2. A schematic representation of the needle inside tissue with a lateral point load F_l applied onto the needle at point c_2.

of the tissue parameter identification method's integration with needle steering is provided in Section IV-D. In Section V, the experimental results and limitations of the proposed method are discussed. Finally, in Section VI, concluding remarks and an outlook on remaining future work are provided.

II. TISSUE YOUNG'S MODULUS IDENTIFICATION

A schematic representation of the proposed method for Young's modulus identification is shown in Fig. 2. The needle is inserted into tissue to a depth d_K. The needle is then laterally displaced by the actuated needle guide. This causes the needle shaft to deflect, which in turn displaces and deforms the tissue surrounding the needle. The tissue is modeled as linearly elastic springs where the spring stiffness is the stiffness of the tissue per unit length squared. The needle, which is constrained by the fixed needle guide at one end, is modeled as a cantilever beam where the needle deflection and its slope are zero at $z = 0$ (see Fig. 2). In order to obtain the tissue Young's modulus K, the principle of conservation of energy is applied, which states that the work that is applied to a system must equal the potential energy that is stored in the system in equilibrium. The work in this case is applied by the actuated needle guide and is related to the measurements of a force/torque sensor that measures F_l, which is correlated to the needle deflection $u(z)$ relative to the needle deflection shape before F_l was applied (assumed to be zero). As discussed later, the needle deflection shape inside tissue can be measured through ultrasound images. The needle deflection shape outside tissue can be measured through a camera or other sensing systems or estimated through an interpolation between the fixed needle guide and the tissue entry point, whose positions are known and act as boundary conditions. The estimated deflection shape of the complete needle is then obtained by piecewise polynomial fitting and interpolation.

In the following, the energy and work terms that represent the needle-tissue system's configuration while a lateral displacement is applied to the needle are introduced. At equilibrium, we have

$$U_s(u) + U_d(u) - V_l = 0 \tag{1}$$

where $U_s(u)$ is the strain energy stored in the bent needle, $U_d(u)$ is the energy stored in the displaced tissue and V_l is the work applied by the actuated needle guide.

1) Strain Energy Stored in the Needle U_s: When the needle is deflected by the actuated needle guide to $u(z = c_2)$, strain energy is stored in the needle which can be formulated as

$$U_s(u) = \frac{EI}{2} \int_0^l u''(z)^2 \, dz \tag{2}$$

where l is the needle length, E and I are the needle Young's modulus and area moment of inertia, respectively, $u(z)$ is the needle deflection shape for $z \in (0, l)$, and $(\cdot)''$ is the second derivative with respect to z.

2) Energy Stored in Tissue U_d: The tissue is modeled as a set of linear elastic virtual springs where the spring stiffness K is the tissue's Young's modulus as expressed in force per unit area. The energy stored in the displaced tissue is

$$U_d(u) = \frac{K}{2} \int_{l-d_K}^l \left(u(z) - u_0(z)\right)^2 \, dz. \tag{3}$$

where $u_0(z)$ is the deflection shape before the lateral displacement is applied to the needle. Since the lateral displacement can be applied in perpendicular direction to the plane of needle deflection, the deflection shape $u_0(z)$ during the Young's modulus identification phase can be assumed to be zero.

3) Work Done by the Actuated Needle Guide V_l: When the actuated needle guide displaces the needle, its displacement at position $z = c_2$ and the lateral force F_l have reached steady state (i.e., are constants) such that the work done by the actuated needle guide can be simply expressed as

$$V_l = F_l u(c_2) \tag{4}$$

where $u(c_2)$ is the lateral needle displacement caused by the actuated guide and F_l is the lateral point load enacted onto the needle at $z = c_2$ that caused this displacement.

Inserting (2), (3), and (4) into (1) gives

$$EI \int_0^l u''(z)^2 \, dz + K \int_{l-d_K}^l u(z)^2 \, dz - 2F_l u(c_2) = 0. \tag{5}$$

Through a trivial re-formulation of (5), the tissue Young's modulus K can now be obtained as

$$K = \frac{2F_l u(c_2) - EI \int_0^l u''(z)^2 \, dz}{\int_{l-d_K}^l u(z)^2 \, dz}. \tag{6}$$

In order to calculate K, the two variables F_l and u_l, and a closed form for $u(z)$ need to be available. F_l is quantified using a force sensor attached to the actuated needle guide and $u(c_2)$ can be obtained from the actuated needle guide. A labeled depiction of the linear actuation unit including force sensor and actuated needle guide are shown in Fig. 6. The final component in (6) that needs to be found is the needle deflection shape $u(z)$ or a closed-form function representation thereof. A suitable representation of $u(z)$ is the piecewise polynomial function

$$\hat{u}(z) = \begin{cases} \hat{u}_1(z) & \text{for } z \in (0, c] \\ \hat{u}_2(z) & \text{for } z \in (c, l) \end{cases} \tag{7}$$

where c is shown in Fig. 2, $\hat{u}_1(z)$ for $z \in (0, c]$ is a polynomial interpolation of the needle deflection shape outside tissue, and $\hat{u}_2(z)$ for $z \in (c, l)$ is a polynomial fit of the needle deflection shape inside tissue.
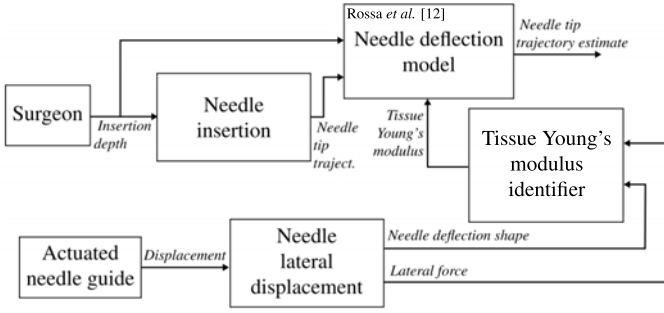
Fig. 3. A block diagram representing the integration of the proposed method for needle-tissue model parameter identification with the prediction of needle deflection.

We found that a third-order polynomial for $\hat{u}_1(z)$ and a second-order polynomial for $\hat{u}_2(z)$ are appropriate, which will be the basis of the rest of the discussion in this section, although higher-order polynomials may be considered for other scenarios. Then, a linear least squares solver is used to fit the second-order polynomial to sampled needle deflection shape measurements. Limiting the polynomial order to two is necessary to prevent over-fitting. The needle deflection shape data is obtained using ultrasound imaging. In order to parameterize $\hat{u}_1(z)$, the four polynomial coefficients $\mathbf{a} = [a_3 \, a_2 \, a_1 \, a_0]^T$ are calculated analytically by using the four known boundary conditions $\hat{u}_1(0) = 0$, $\hat{u}_1'(0) = 0$, $\hat{u}_1(c) = \hat{u}_2(c)$ and $\hat{u}_1'(c) = \hat{u}_2'(c)$ where $(\cdot)'$ is the first derivative with respect to z. To calculate $\mathbf{a}$, the linear system of equations

$$\begin{bmatrix} 0 & 0 & 0 & 1 \\ 0 & 0 & 1 & 0 \\ c^3 & c^2 & c & 0 \\ 3c^2 & 2c & 1 & 0 \end{bmatrix} \begin{bmatrix} a_3 \\ a_2 \\ a_1 \\ a_0 \end{bmatrix} = \begin{bmatrix} 0 \\ 0 \\ \hat{u}_2(c) \\ \hat{u}_2'(c) \end{bmatrix} \tag{8}$$

is solved.

At this point, $\hat{u}(z)$ is identified and can be inserted into (6) in order to obtain the tissue Young's modulus K.

III. INTEGRATION WITH PREDICTION OF NEEDLE DEFLECTION

This section presents the integration of the proposed tissue Young's modulus intraoperative identification method with an existing needle deflection model for the prediction of needle deflection. The deflection modeling is based on the method proposed by Rossa *et al.* [12]; it should be noted that any other deflection model that is designed based on mechanics of needle-tissue interaction, and thus in need of the knowledge of tissue Young's modulus, can be combined with our proposed method. The proposed integration does not require modifications to the needle deflection model proposed in [12], which makes the proposed research appealing from a practical perspective.

Fig. 3 illustrates the integration of the Young's modulus estimation with the needle insertion procedure. The shown block diagram consists of three components, namely the actuated needle, the intraoperative tissue Young's modulus identification, and the needle deflection model.
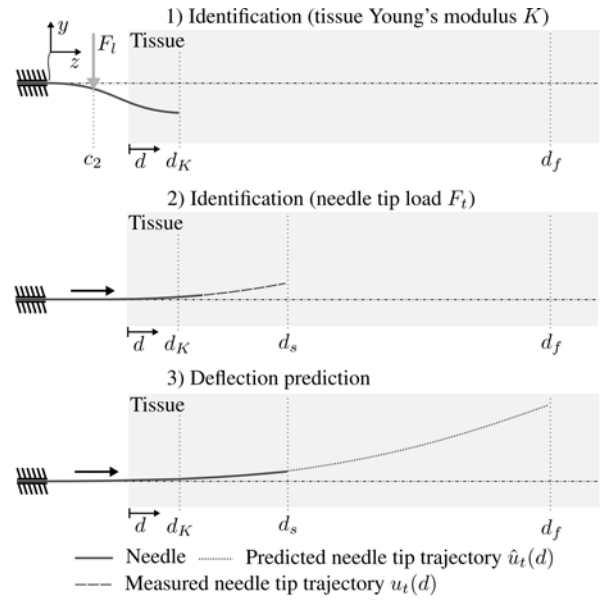

Fig. 4. The three phases of one needle insertion. d_K is the insertion depth at which the tissue Young's modulus K is identified, d_s is the insertion depth up to which the needle deflection is measured for identification of the tip load F_t and d_f is the final insertion depth.

The needle can be actuated by two different means: insertion and lateral displacement (enacted by the actuated needle guide). The former directly influences the needle deflection shape, which can be measured during insertion using ultrasound (US) imaging.

Fig. 4 depicts a schematic representing the chronological succession of three steps towards predicting needle deflection; 1) identifying tissue Young's modulus K, 2) identifying the needle tip load F_t and 3) predicting needle deflection.

1) Identification of tissue Young's modulus K: When the insertion depth d_K is reached, the needle insertion is paused and the needle is laterally displaced by the actuated needle guide. The needle deflection shape inside tissue $u(z)$ is then measured using transverse ultrasound images. A force sensor attached to the actuated needle guide measures the lateral force F_l applied by the guide to the needle. Subsequently, the tissue Young's modulus K is identified based on the aforementioned measurements $u(z)$ and F_l.

2) Identification of needle tip load F_t: After the lateral needle displacement is removed, the needle is further inserted up to depth d_s while the needle tip trajectory $u_t(d)$ is recorded using transverse ultrasound images. The tip load F_t can then be identified using a modified version of the deflection model that takes as input $u_t(d)$ and the previously identified K.

3) Prediction: In the third step, both K and F_t are supplied to the needle deflection model in order to predict the needle deflection beyond depth d_s.

A. Needle Deflection Model

To model the needle deflection during insertion, the model introduced by Rossa *et al.* [12] is used. A schematic representation of the modeled needle-tissue interactions is illustrated in Fig. 5. It shows tissue compression along the needle modeled
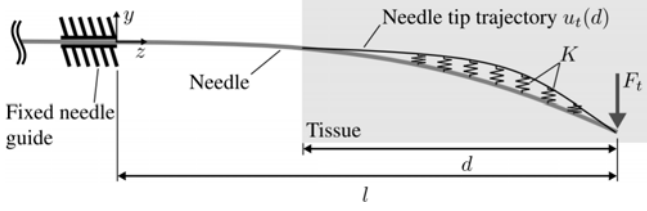
Fig. 5. A schematic of the modeled needle-tissue interactions as a sequence of linear elastic springs modeling tissue displacement and a point load at the needle tip modeling the tip cutting tissue.

as a sequence of linear elastic springs with stiffness K and the needle tip cutting of tissue as a transverse point load F_t. The deflection model is based on an energy-based formulation of the needle-tissue interactions that consists of the sum of the energy stored in the system, and the work exerted onto the needle-tissue system. To solve this energy formulation for the needle deflection, the Rayleigh-Ritz method is employed. This variational method uses a finite sum of shape functions, with which the energy formulation can be re-formulated into a linear system of equations. The solution to this linear system of equations represents an approximation to the needle shape.

1) Needle-tissue Interaction Modeling: Here, the modeling of the various energy components representing the needle-tissue system during insertion are introduced as the system potential

$$\Pi(u,d) = U_s(u,d) + U_d(u,d) + V_c \tag{9}$$

where $U_s(u,d)$ is the strain energy due to the bending of the needle and $U_d(u,d)$ is the energy stored in the displaced tissue. V_c is the work done by the tip force F_t. Expressions for $U_s(u,d)$ and $U_d(u,d)$ can be found in (2) and (3), respectively.

a) Work Done by the Needle Tip Force F_t: As in each discrete insertion step a steady state is assumed, the tip force can be expressed as [12]

$$V_c = F_t u(l,d) \tag{10}$$

where $u(l,d)$ is the needle tip deflection. After inserting (2), (3) and (10) into (9), we obtain

$$\begin{aligned}
\Pi(u,d) &= \int_0^l \frac{EI}{2}\left(\frac{\partial^2 u(z,d)}{\partial z^2}\right)^2 dz \\
&+ \frac{K}{2}\int_{l-d}^l \left(u(z,d) - u_t(d,z)\right)^2 dz \\
&- F_t u(l,d)
\end{aligned} \tag{11}$$

2) Needle Deflection: To obtain an approximation for the needle shape $u(z,d)$ at insertion depth d, the system potential formulated in (11) is re-formulated into a linear system of equations according to the Rayleigh-Ritz method. The first step is to obtain a finite sum of weighted shape functions approximating $u(z,d)$ as [27]

$$u_n(z,d) = \sum_{i=1}^n q_i(z)g_i(d), \tag{12}$$

where $q_i(z)$ is the ith shape function and $g_i(d)$ is the ith weight coefficient assigned to $q_i(z)$. The ith shape function $q_i(z)$ is expressed as

$$\begin{aligned}
q_i(z) = \frac{1}{\kappa_i}&\left(\sin(\beta_i\frac{z}{l}) - \sinh(\beta_i\frac{z}{l})\right. \\
&\left. - \gamma_i\left[\cos(\beta_i\frac{z}{l}) - \cosh(\beta_i\frac{z}{l})\right]\right).
\end{aligned} \tag{13}$$

κ_i and γ_i are computed as

$$\begin{aligned}
\gamma_i &= \frac{\sin\beta_i + \sinh\beta_i}{\cos\beta_i + \cosh\beta_i} \\
\kappa_i &= \sin\beta_i - \sinh\beta_i - \gamma_i(\cos\beta_i - \cosh\beta_i). \tag{14}
\end{aligned}$$

The values for the coefficients β_i for a cantilever beam (clamped-free) are $\beta_1 = 1.857$, $\beta_2 = 4.695$, $\beta_3 = 7.855$, $\beta_4 = 10.996$, and $\beta_i \simeq \pi(i-1/2)$ for $i > 4$.

The sum of weighted shape functions u_n (12) is now inserted into (11):

$$\begin{aligned}
\Pi(u_n) &= \frac{EI}{2}\int_0^l \left(\sum_{i=1}^n q_i''(z)g_i(d)\right)^2 dz \\
&+ \frac{K}{2}\int_{l-d}^l \left(\sum_{i=1}^n q_i(z)g_i(d) - u_t(z,d)\right)^2 dz \\
&- F_t\sum_{i=1}^n q_i(l)g_i(d)
\end{aligned} \tag{15}$$

where $(\cdot)''$ denotes the second derivative with respect to z.

Finally, we want to express (15) as a linear system of equations in order to solve for the unknown weight coefficients $g_i(d)$. This is achieved through the principle of minimum potential such that $\frac{\partial \Pi(u)}{\partial g_j} = 0$ for $j = 1,\ldots,n$. Thus, the final step is to take the partial derivative of (15) with respect to all $g_j(d)$ considering that $q_i(l) = q_j(l) = 1$, $\forall i,j$, (see (13)) and that $q_j(c_2)$, $\forall j$, is known:

$$\begin{aligned}
\frac{\partial \Pi(u_n)}{\partial g_j(d)} =& EI\int_0^l \left(\sum_{i=1}^n q_i''(z)g_i(d)\right)q_j''(z)\,dz \\
&+ K\int_{l-d}^l \left(\sum_{i=1}^n q_i(z)g_i(d) - u_t(d,z)\right)q_j(z)\,dz \\
&- F_t = 0.
\end{aligned} \tag{16}$$

After re-arranging and simplifying (16), we have

$$\sum_{i=1}^n \phi_{ji}g_i(d) - \omega_j - F_t = 0 \tag{17}$$

with

$$\begin{aligned}
\phi_{ji}(z) &= EI\int_0^l q_i''(z)q_j''(z)\,dz + K\int_{l-d}^l q_i(z)q_j(z)\,dz \\
\omega_j(z) &= K\int_{l-d}^l u_t(d,z)q_j(z)\,dz.
\end{aligned}$$

Finally, (17) is converted to the matrix formulation

$$\begin{bmatrix} \phi_{11} & \cdots & \phi_{1n} \\ \vdots & \ddots & \vdots \\ \phi_{n1} & \cdots & \phi_{nn} \end{bmatrix}\mathbf{g}(d) = F_t\begin{bmatrix} 1 \\ \vdots \\ 1 \end{bmatrix} + \begin{bmatrix} \omega_1 \\ \vdots \\ \omega_n \end{bmatrix} \tag{18}$$

and can then be solved for $\mathbf{g}(d) = \begin{bmatrix} g_1 & \dots & g_n \end{bmatrix}^T$ and inserted into (12) to obtain $u_n(z,d)$, the approximated needle shape.

It should be noted that the needle length l is considered variable in this model re-derivation as opposed to [12], which allows for a faster numerical solution.

B. Needle Tip Force Identification

The second parameter required by the deflection model is a cutting-related force at the needle tip, which is the primary cause for needle deflection. As the needle is inserted, the beveled needle tip cuts, displaces and therefore compresses tissue asymmetrically. The one-sided tissue compression causes the needle to deflect in the direction of the bevel. The force F_t is assumed to be constant throughout insertion. Generally, due to the needle deflection slope, the relation between the needle tip load as expressed in the needle tip frame is $F_t' = F_t \cos(\theta)$ where θ is the needle tip deflection slope. Since, however, θ is small ($< 15°$), it can be assumed that $\cos(\theta) \sim 1$. To identify F_t, a re-formulated version of the deflection model presented in the previous section is employed. The re-formulated model takes as input the needle tip deflection $u_t(z)$ and the parameter tissue Young's modulus K. The model will henceforth be referred to as *tip force model*. Needle tip deflection data is obtained as the needle is inserted during the identification step introduced in Section III. The tip force model is established by exploiting a special case of (13), which occurs at $z = l$ where $q_i(l) = 1 \, \forall \, i$ such that

$$u_n(l,d) = \sum_{i=1}^{n} g_i(d) = u_t(d). \tag{19}$$

Now, (18) is expanded to $n+1$ equations [12] to obtain

$$\begin{bmatrix} \phi_{11} & \cdots & \phi_{1n} & -1 \\ \vdots & \ddots & \vdots & \vdots \\ \phi_{n1} & \cdots & \phi_{nn} & -1 \\ 1 & \dots & 1 & 0 \end{bmatrix} \underbrace{\begin{bmatrix} \mathbf{g} \\ F_t \end{bmatrix}}_{\mathbf{g}^*} = \begin{bmatrix} \omega_1 \\ \vdots \\ \omega_n \\ 0 \end{bmatrix} + \begin{bmatrix} 0 \\ \vdots \\ 0 \\ u_t \end{bmatrix}. \tag{20}$$

Finally, (20) can be solved for $\mathbf{g}^* = \begin{bmatrix} \mathbf{g} & F_t \end{bmatrix}^T$ in order to obtain the tip force F_t for a given tip deflection $u_t(d)$. To estimate the tip force that is to be supplied to the deflection model, the tip force samples calculated from measured needle tip deflection samples at insertion depths d_K to d_s are averaged.

IV. EXPERIMENTAL STUDIES

In this section, two experimental studies are presented. In the first study, the concept proposed in Section II for tissue Young's modulus identification is validated and in the second study, the feasibility for incorporation with deflection modeling and prediction is presented.

A. Experimental Needle Insertion Setup

The experimental setup used for both studies presented in Section IV-C and Section IV-D is introduced in this section. The setup is depicted in Fig. 6 and is designed to mimic the clinical conditions found during prostate brachytherapy. It consists of a tissue sample into which a standard 18 gauge brachytherapy needle is inserted using the Hand-held Needle
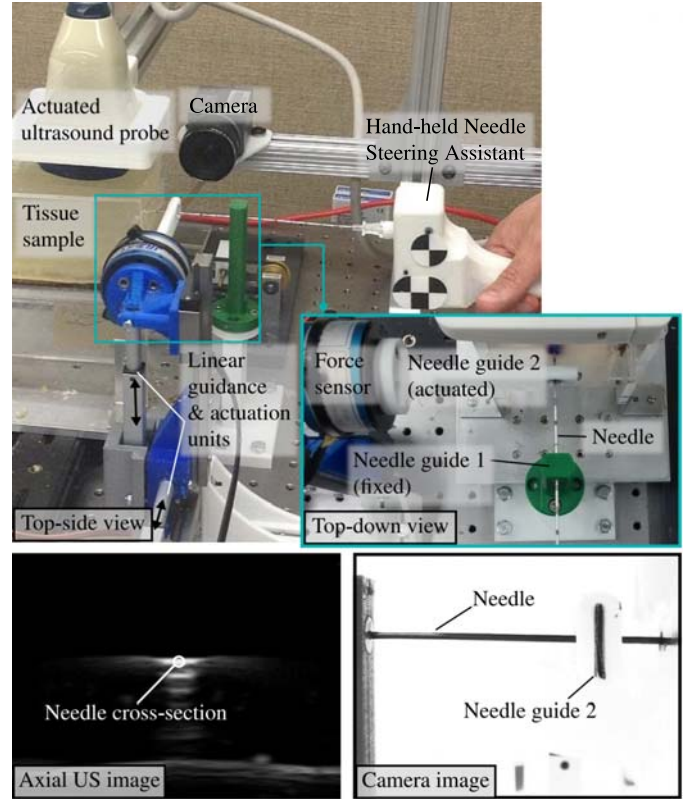

Fig. 6. The experimental setup used for semi-manual needle insertion through a Hand-held Needle Steering Assistant [12]. The setup is designed to mimic the clinical conditions of prostate brachytherapy and is used in this work for experimental validation.

Steering Assistant (HNSA) [12], the lateral guidance and actuation units responsible for lateral needle actuation, an ultrasound imaging system, a camera, and a force sensor. The needle is laterally constrained by needle guide 1 and laterally actuated by needle guide 2. Guide 2 can be moved on a plane normal to the axial needle direction via two linear guidance and actuation units that each consist of a Miniature Linear Guide (Type SSEBV16-150, MISUMI Group Inc., Tokyo, Japan) and a L16 Miniature Linear Actuator (Actuonix Motion Devices Inc., Victoria, BC, Canada) mounted in series. One actuation unit is mounted horizontally and the other vertically. The vertical unit is used to displace the needle while the horizontal unit is in this work only used to horizontally align needle guide 2 with needle guide 1. The forces caused by lateral needle displacement are measured by a JR3 force sensor (Type 50M31A3-I25, JR3 Inc., Woodland, CA, USA) mounted between the linear actuation units and needle guide 2. The sensor registers forces in vertical and horizontal directions.

The needle is attached to the HNSA with which it is inserted manually into tissue. During insertion, the HNSA's relative position to the tissue container and therefore the current insertion depth is measured using an optical tracker. Further details on the HNSA are given in [12].

A clinical ultrasound (US) system obtains axial images of the needle cross-section inside tissue. The US system consists of a US transducer (Model 4DL14-5/38 Linear 4D, Ultrasonix, Richmond, BC, Canada) and a diagnostic US system (Model

SonixTOUCH, Ultrasonix, Richmond, BC, Canada), which generates US images from sonography data acquired by the US transducer. A sample US image containing a bright spot that marks the needle cross-section is shown in Fig. 6. The US transducer is mounted via a crossbar structure onto an actuated linear stage, which restricts the US transducer to be moved only in parallel to the axial needle direction. The actuated US transducer can be controlled such that it tracks the needle tip during insertion in order to observe the needle tip trajectory or to sweep along a given distance e.g., to measure the needle deflection shape. The acquired US image sequence is then analysed to obtain discrete samples of the needle tip trajectory or deflection shape inside tissue using a modified version of the algorithm presented in [28]. The pixel to millimeter conversion ratio for US images is 0.051 millimeters per pixel. The scanning depth of the US system was set to 45 mm, the imaging width was 32 mm such that the vertical and horizontal pixel to mm conversion ratio is equal in horizontal and vertical direction. The US image resolution is 625×750 pixels.

A camera (Model XCD-SX90CR, Sony Corporation, Tokyo, Japan) captures image sequences from the right side of the needle. The camera image sequences are used to accurately measure the vertical displacement of needle guide 2 during each experimental trial and thus the needle deflection $u(c_2)$. A basic template matching routine that tracks the location of the actuated guide within an image sequence measures the vertical displacement. The pixel to millimeter conversion ratio for camera images is 0.051 millimeters per pixel. The displacement of the actuated needle guide is obtained through camera images due to the high positional accuracy needed for obtaining the mechanical work V_l (see (4)) induced by the actuated needle guide. The linear actuators provide an accuracy of ± 0.3 mm.

B. Tissue Indentation Experiments

In Section IV-C and Section IV-D, two phantom tissue samples with different Young's moduli are used. Both samples are made from Plastisol (Type Super Soft Plastic, M-F Manufacturing Co., Inc, Fort Worth, TX, USA) where plastic softener is used to adjust the tissue stiffness and thus its Young's modulus. In order to establish a ground truth for the two tissue samples' Young's moduli, an independent measurement is needed. The applied method is a tissue indentation test where a blunt cylindrical punch indents the tissue to a defined depth while the indentation force is measured. The indentation setup is shown in Fig. 7a. During an indentation experiment, the indenter is advanced with a constant velocity of 1 mm/s up to a depth $x_f = 3.5$ mm. The Young's modulus is then calculated with the relation [23]

$$K = \frac{(1-\nu^2)F}{2ax\kappa} \tag{21}$$

where x and F are the indentation depth and force, respectively, a is the indenter radius, ν is Poisson's ratio and κ represents a constant, which is unity for a semi-infinite body (see Fig. 7b). The tissue is assumed linearly elastic, homogeneous and incompressible. Thus, Poisson's ratio ν is 0.5. As the dimensions of our tissue sample (width 70 mm
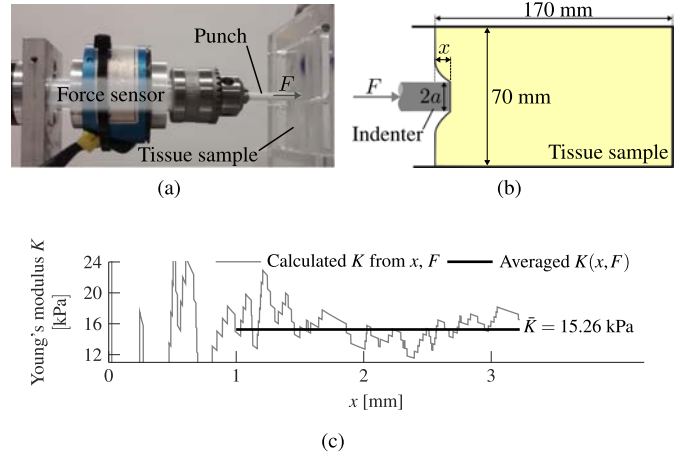

Fig. 7. (a) The experimental setup for the indentation test and (b) a schematic showing the tissue indentation and assigned dimensional labels where $a = 2.1$ mm is the radius of the indenter and F is the force resulting in the indentation depth x. (c) The result of one indentation test run.

and depth 170 mm) are large with respect to the indenter and a maximum indentation depth of $x_f = 3.5$ mm, it is presumed that semi-infinite conditions apply. A sample plot for tissue sample one that plots the Young's modulus K against the indentation depth x is shown in Fig. 7c. Six runs of the above described experiment are carried out and $\bar{K}$, the averaged K is calculated for each run. Finally, the mean of each run's $\bar{K}$ is taken to obtain the final values for the tissue Young's modulus K_{REF}. The measured K_{REF} is 16.23$\pm$2.73 kPa for tissue sample 1, and for tissue sample 2 it is 12.61$\pm$2.63 kPa.

C. Validation of Young's Modulus Identification

Three experimental trials were carried out where the three insertion depths d_K of 20 mm, 30 mm and 40 mm are considered for trial one, two and tree, respectively. For each trial, six runs were performed. Relatively shallow insertion depths are chosen since it is desired to carry out this identification routine early on during insertion. A parameterized needle deflection model will then be available for needle steering algorithms earlier during insertion. Multiple trials with varying insertion depth are selected to show the robustness of the proposed method to different insertion depths. A rather small lateral needle displacement of 1.2 mm at $z = c_2$ is chosen to comply with the assumption that the tissue is linearly elastic.

The needle used for the experiments was a standard 18g brachytherapy needle (Type RP-1100-1820, Riverpoint Medical, Portland, OR, USA), which has a Young's modulus of $E = 200$ GPa, an outer radius of 0.635 mm, an inner radius of 0.5 mm, and a bevel angle of 20°. The needle was inserted into tissue sample 1 through the fixed and actuated needle guides as shown in Fig. 6. Each experimental run was carried out in the following sequence:
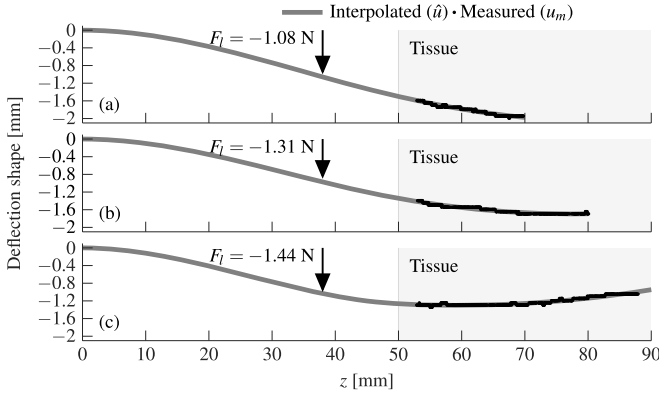
Fig. 8. The measured needle deflection shape inside tissue and estimated deflection shape for insertion depths (a) $d = 20$ mm, (b) $d = 30$ mm and (c) $d = 40$ mm.

TABLE I

RESULTS OF THE TISSUE YOUNG'S MODULUS IDENTIFICATION. K_{ID} IS THE MEAN OF THE IDENTIFIED YOUNG'S MODULUS OVER 6 EXPERIMENTAL RUNS AND σ IS THE STANDARD DEVIATION. h IS THE TEST DECISION OF A TWO-SAMPLE t-TEST INDICATING WHETHER THE DIFFERENCE BETWEEN K_{REF} AND K_{ID} IS SIGNIFICANTLY DIFFERENT (r) OR NOT ($\bar{r}$).

Insertion depth d_K [mm]	K_{ID} [kPa]	σ	$\|K_{REF} - K_{ID}\|$ [kPa]	t-test	
				h	p-value
20	16.53	2.63	0.3	$\bar{r}$	0.85
30	14	2.62	2.23	$\bar{r}$	0.18
40	13.94	3.15	2.29	$\bar{r}$	0.21

1) Displace needle vertically at $z = c_2$ by -1.2 mm using actuated needle guide and hold displacement.
2) Move actuated US transducer from needle entry point ($z = c$) to needle tip ($z = l$) at velocity 1 mm/s to obtain an image sequence of needle cross-sections at varying depth.
3) Remove vertical needle displacement once the US transducer reaches the needle tip.

Fig. 8 shows the measured needle deflection shape inside tissue (u_m) with applied lateral force F_l at $z = c_2$ and the interpolated deflection shape $\hat{u}(z)$ determined using the method described in Section II. The measured deflection shape's noise is very low and the error is essentially limited to the pixel quantization error of the ultrasound images (0.05 mm). This results in a good quality of fit with a residual sum of squares (RSS) of 0.14 mm² for Fig. 8a, 0.18 mm² for Fig. 8b, and 0.29 mm² for Fig. 8c. The RSS for all other runs is of the same magnitude.

To identify the tissue Young's modulus K, the interpolated needle deflection shape $\hat{u}(z)$, the applied lateral force F_l, and the measured needle deflection $u(c_2)$ are inserted into (6). The resulting estimate for the Young's modulus K_{ID} is given in Table I as an average over the six runs. The standard deviation σ ranges from approximately 16% to 23% of K_{ID}. The absolute error between the Young's modulus ground truth K_{REF} and the estimated K_{ID} is lowest for insertion depth $d_K = 20$ mm with 0.3 kPa and highest for $d_K = 40$ mm with 2.29 kPa. A two-sample t-test decision h, which determines
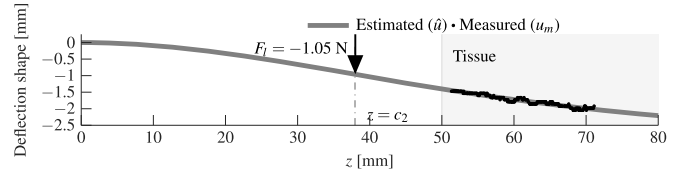

Fig. 9. The measured needle deflection shape inside tissue and predicted deflection shape for insertion depth $d = 30$ mm (20 mm measured) and tissue sample 2.
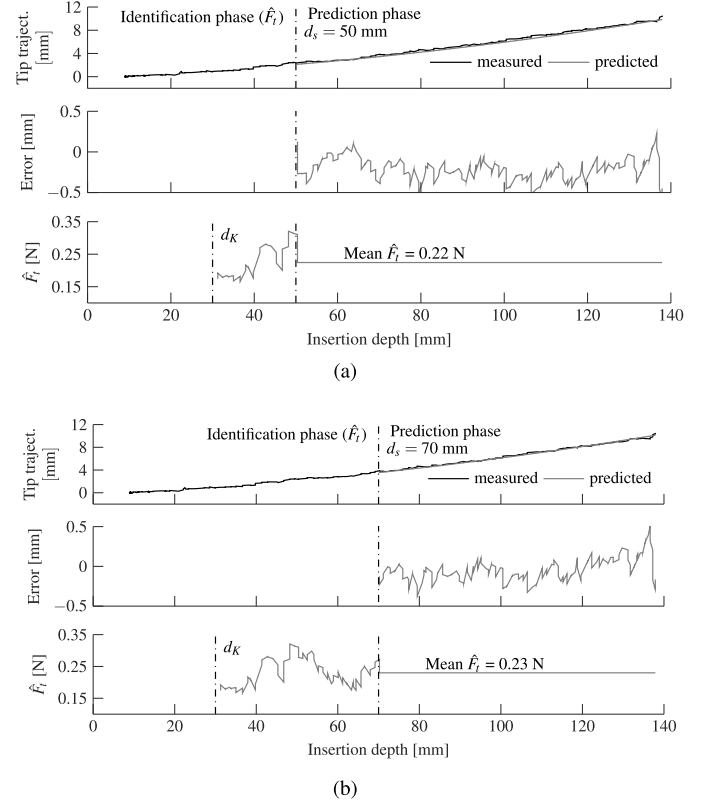

Fig. 10. A sample insertion with a phase for identifying the tip force F_t and a phase for the prediction of the needle tip trajectory based on the tip force estimate $\hat{F}_t$ obtained during the identification phase. The switch from tip force identification to tip trajectory prediction was done at insertion depths (a) $d_s = 50$ mm and (b) $d_s = 70$ mm.

whether K_{ID} and K_{REF} are significantly different and the test's p-value show that for none of the trials, K_{ID} and K_{REF} are significantly different at a significance level of 5%.

D. Prediction of Needle Deflection

The prediction performance of the deflection model re-introduced in Section III-A is evaluated when the deflection model is calibrated using the proposed method for Young's modulus identification. For this study, we use tissue sample 2.

The sequence of steps described in Section III is followed towards predicting needle deflection. First, the tissue Young's modulus of tissue 2 is identified using the proposed method. Fig. 9 shows the measured needle deflection shape inside tissue and the resulting deflection shape prediction. The identified tissue Young's modulus is $K_{ID} = 10.36$ kPa.

For evaluating the final two steps that are needle tip force identification and deflection prediction, six insertions

Switching depth d_s	Insertion depth d	Mean $\hat{u}_t(d)$	Mean $u_t(d)$	MAE
50	80	4.13±0.49	4.58±0.21	0.48±0.26
	100	5.86±0.66	6.54±0.26	0.72±0.53
	120	7.80±0.93	8.62±0.28	1.02±0.59
	140	9.73±1.16	10.56±0.47	1.24±0.59
70	80	4.38±0.30	4.58±0.21	0.22±0.17
	100	6.24±0.37	6.54±0.26	0.32±0.30
	120	8.30±0.53	8.62±0.28	0.50±0.34
	140	10.36±0.66	10.56±0.47	0.73±0.40

are carried out to a final insertion depth of $d_f = 140$ mm while tracking the needle tip deflection with the actuated US transducer. The insertion data is then used to identify F_t from insertion depth $d_K = 30$ mm to d_s.

After depth d_s is reached, the needle tip trajectory $\hat{u}(d)$ is predicted using the identified K_{ID} and F_t. It should be noted that F_t is dependent on K_{ID} as is evident from (20). In Fig. 10, sample needle tip trajectories, the identified F_t and tip trajectory prediction are plotted for two different depths d_s. For both considered d_s, the error between the predicted and measured tip trajectory remains below 0.5 mm. A statistical comparison between the measured and predicted needle tip trajectory is provided in Table II. The mean measured ($u_t(d)$) and predicted ($\hat{u}_t(d)$) needle tip deflections for $i = 1, \ldots, 6$ insertions and at four insertion depths are evaluated along with the mean absolute error (MAE $= \frac{1}{6}\sum_{i=1}^{6}|\hat{u}_{t,i}(d) - u_{t,i}(d)|$) and the respective standard deviations for all listed quantities. Results for both $d_s = 50$ mm and $d_s = 70$ mm are tabulated. The results show a larger MAE for the tip deflection prediction when the identification is stopped at $d_s = 50$ mm. Moreover, for $d_s = 70$ mm, the MAE remains below 1 for all listed insertion depths. This is not the case for $d_s = 50$ mm where the maximum MAE is 1.24 mm at insertion depth 140 mm.

V. DISCUSSION

The results presented is Section IV-C show that the tissue Young's modulus can be accurately identified with the proposed method for intraoperative tissue Young's modulus identification using a laterally actuated needle. The fact that the identification method can be applied reliably at varying insertion depths provides additional flexibility with respect to clinical application. With an estimate of the tissue Young's modulus being available early on during insertion, deflection models can potentially be calibrated earlier and a full prediction of deflection can be provided earlier during insertion, which is advantageous for needle steering.

The sources of error during the identification procedure are the US-based needle shape measurement, the measurement of the lateral force F_l, and the measurement of the lateral displacement enacted by the actuated needle guide. The highest measurement error occurs during force measurement as the

force sensor's dynamic range of 100 N is relatively high with respect to the measured force magnitude of approximately 1 N. When considering that the standard deviation is consistent for both Young's modulus identification and independent measurement, and that force is the only common measurement among the two methods, then the inaccuracy of our proposed method can be attributed to the force measurement. Therefore, the accuracy of our proposed method can be significantly increased with a more appropriate force sensor. Moreover, the standard deviation of approximately 16% is an indicator of a reliably identified Young's modulus.

The accuracy of the proposed method is on par with other state of the art approaches to identify the Young's modulus, such as indentation and ultrasound-based elastography under similar experimental conditions. Lu et al. [24] proposed a hand-held indentation system, where the difference between the ground truth and the identification via indentation probe was found to be 0.48 kPa with phantom tissue. Fu et al. [25] investigated the identification of tissue Young's modulus using B-scan ultrasound. The identified average Young's modulus was 10 kPa with a range of 9-12 kPa. The difference to the ground truth was 10.4%, or 1.04 kPa. In both above approaches, the ground truth was established using mechanical stress-strain tests. Our proposed method shows an average difference between ground truth and identified Young's modulus of 1.61 kPa for the three considered needle insertion depths.

Experiments showed that the reliability of the proposed identification method is also highly dependent on the accuracy of the US-based needle shape measurement. The quality of the needle curvature fit inside tissue is dependent on the amount of noise present in the needle shape measurement and therefore the calculated potential energy. A more robust method for estimating the needle shape from noisy needle shape measurements (e.g., considering beam-related models for needle shape estimation) can be a focus of future work.

The prediction accuracy of the needle tip trajectory given in Section IV-D is dependent on the depth d_s at which the switch to deflection prediction occurs. When the tip force F_t is identified up to a depth of 50 mm, the mean absolute error between measured and estimated needle tip trajectory exceeds 1 mm as opposed to when $d_s = 70$ mm where the MAE does not exceed 1 mm. The increased error for $d_s = 50$ mm can be attributed to the noise present in the needle tip deflection measurement that is reflected in $\hat{F}_t(d)$ for $d \in [d_K, d_s]$ (see Fig. 10). When more samples of $\hat{F}_t$ are present (e.g., the distance d_K to d_s is larger), the mean of $\hat{F}_t$ for $d \in [d_K, d_s]$ gains in accuracy. Therefore, the predicted needle tip trajectory's accuracy could be significantly improved with a more accurate deflection measurement while the depth d_s can then be reduced. As illustrated in Section III, the Young's modulus identification using a laterally actuated needle is not time consuming with an estimated identification procedure duration of two to three seconds during which needle insertion needs to be paused. Thus, the method integrates well with clinical practice.

Biological pelvic tissues as well as any other region of the body are structured in layers from the perspective of the needle and therefore varying Young's moduli are expected at

various insertion depths. The presented method of Young's modulus identification does not take this into account. In order to mitigate this limitation, the identification procedure could be carried out at multiple insertion depths where a change of tissue layers occurs. In the case of prostate brachytherapy, the identification procedure would have to be carried out twice during the first of roughly 20 insertions for the pre-prostate tissue layer and the prostate. The changing tissue stiffness among layers should then be to a certain extent reflected in the measured needle deflection resulting from lateral force application such that varying Young's moduli can be identified. Moreover, muscle tissue may present some directional dependence based on the muscle's parallel or perpendicular fiber alignment with the direction of lateral needle displacement. To explore the tissue characteristics of biological tissue using our method, the identification procedure may be carried out in multiple lateral directions to identify the fiber alignment of the muscle tissue.

VI. Conclusion

This paper proposes an intraoperative method for the identification of tissue Young's modulus during needle insertion using a laterally actuated needle. Experimental evaluation shows a close match between the identified and independently measured tissue Young's modulus. Furthermore, the integration with the deflection-model-based prediction of the needle tip trajectory is presented. The high accuracy of the predicted needle tip trajectory demonstrates the successful calibration of a deflection model found in the literature using the proposed method for Young's modulus identification. Our future work will concern using lateral needle actuation as "control input" for needle steering, not just for tissue Young's modulus identification. The concept of lateral actuation is part of the development of a novel robotic assistant system for needle insertion that is able to manipulate the needle deflection trajectory during insertion using a combination of axial needle rotation and lateral needle displacement. Thus, the successful validation of the introduced method is an important step towards the development of a complete robotic assistant system for needle insertion that is able to identify all necessary parameters for model-informed needle steering and deflection control.

References

[1] C. Simone and A. Okamura, "Modeling of needle insertion forces for robot-assisted percutaneous therapy," in *Proceedings of the 2002 IEEE International Conference on Robotics and Automation*, vol. 2, May 2002, pp. 2085–2091.

[2] A. Okamura, C. Simone, and M. O'Leary, "Force modeling for needle insertion into soft tissue," *IEEE Transactions on Biomedical Engineering*, vol. 51, no. 10, pp. 1707–1716, Oct. 2004.

[3] S. Misra, K. B. Reed, A. S. Douglas, K. T. Ramesh, and A. M. Okamura, "Needle-tissue interaction forces for bevel-tip steerable needles," in *Proceedings of the 2nd Biennial IEEE/RAS-EMBS International Conference on Biomedical Robotics and Biomechatronics, BioRob 2008*, 2008, pp. 224–231.

[4] S. Misra, K. B. Reed, B. W. Schafer, K. T. Ramesh, and A. M. Okamura, "Observations and models for needle-tissue interactions," in *Proceedings of the 2009 IEEE International Conference on Robotics and Automation*, May 2009, pp. 2687–2692.

[5] S. Misra, K. B. Reed, B. W. Schafer, K. T. Ramesh, and A. M. Okamura, "Mechanics of flexible needles robotically steered through soft tissue," *The International Journal of Robotics Research*, vol. 29, no. 13, pp. 1640–1660, Nov. 2010.

[6] R. Roesthuis, Y. V. Veen, A. Jahya, and S. Misra, "Mechanics of needle-tissue interaction," in *2011 IEEE/RSJ International Conference on Intelligent Robots and Systems (IROS)*. IEEE, Sep. 2011, pp. 2557–2563.

[7] A. Asadian, M. R. Kermani, and R. V. Patel, "A novel force modeling scheme for needle insertion using multiple kalman filters," *IEEE Transactions on Instrumentation and Measurement*, vol. 61, no. 2, pp. 429–438, 2012.

[8] R. J. Roesthuis, M. Abayazid, and S. Misra, "Mechanics-based model for predicting in-plane needle deflection with multiple bends," in *Proceedings of the 2012 IEEE RAS and EMBS International Conference on Biomedical Robotics and Biomechatronics*, June 2012, pp. 69–74.

[9] M. Khadem, B. Fallahi, C. Rossa, R. S. Sloboda, N. Usmani, and M. Tavakoli, "A mechanics-based model for simulation and control of flexible needle insertion in soft tissue," in *Proceedings of the 2015 IEEE International Conference on Robotics and Automation (ICRA)*. IEEE, may 2015, pp. 2264–2269.

[10] T. Lehmann, C. Rossa, N. Usmani, R. S. Sloboda, and M. Tavakoli, "A Real-Time Estimator for Needle Deflection During Insertion Into Soft Tissue Based on Adaptive Modeling of Needle-Tissue Interactions," *IEEE/ASME Transactions on Mechatronics*, vol. 21, no. 6, pp. 2601–2612, 2016.

[11] C. Rossa, M. Khadem, R. Sloboda, N. Usmani, and M. Tavakoli, "Adaptive Quasi-Static Modelling of Needle Deflection During Steering in Soft Tissue," *IEEE Robotics and Automation Letters*, vol. 1, no. 2, pp. 916–923, 2016.

[12] C. Rossa, N. Usmani, R. Sloboda, and M. Tavakoli, "A Hand-Held Assistant for Semiautomated Percutaneous Needle Steering," *IEEE Transactions on Biomedical Engineering*, vol. 64, no. 3, pp. 637–648, 2017.

[13] M. Khadem, C. Rossa, N. Usmani, R. S. Sloboda, and M. Tavakoli, "A Two-body Rigid/Flexible Model of Needle Steering Dynamics in Soft Tissue," *IEEE/ASME Transactions on Mechatronics*, vol. 21, no. 5, pp. 2352–2364, 2016.

[14] W. Park, J. S. Kim, Y. Zhou, N. Cowan, A. Okamura, and G. Chirikjian, "Diffusion-Based Motion Planning for a Nonholonomic Flexible Needle Model," in *Proceedings of the 2005 IEEE International Conference on Robotics and Automation*, no. April, 2005, pp. 4600–4605.

[15] R. J. Webster, J. S. Kim, N. J. Cowan, G. S. Chirikjian, and A. M. Okamura, "Nonholonomic modeling of needle steering," *Int. J. Rob. Res.*, vol. 25, no. 5-6, pp. 509–525, May 2006.

[16] D. Glozman and M. Shoham, "Image-guided robotic flexible needle steering," *IEEE Transactions on Robotics*, vol. 23, no. 3, pp. 459–467, 2007.

[17] M. Abayazid, R. Roesthuis, R. Reilink, and S. Misra, "Integrating Deflection Models and Image Feedback for Real-Time Flexible Needle Steering," *IEEE Transactions on Robotics*, vol. 29, no. 2, pp. 542–553, Apr. 2013.

[18] S. Patil, J. Burgner, R. J. Webster, and R. Alterovitz, "Needle steering in 3-D Via rapid replanning," *IEEE Transactions on Robotics*, vol. 30, no. 4, pp. 853–864, 2014.

[19] B. Fallahi, M. Khadem, C. Rossa, R. Sloboda, N. Usmani, and M. Tavakoli, "Extended Bicycle Model for Needle Steering in Soft Tissue," in *Proceedings of the 2015 IEEE/RSJ International Conference on Intelligent Robots and Systems (IROS)*, October 2015, pp. 4375–4380.

[20] P. Moreira and S. Misra, "Biomechanics-Based Curvature Estimation for Ultrasound-guided Flexible Needle Steering in Biological Tissues," *Annals of Biomedical Engineering*, vol. 43, no. 8, pp. 1716–1726, 2014.

[21] S. Misra, K. T. Ramesh, and A. M. Okamura, "Modeling of Tool-Tissue Interactions for Computer-Based Surgical Simulation: A Literature Re-

view," *Presence: Teleoperators and Virtual Environments*, vol. 17, no. 5, pp. 463–491, 2008.

[22] C. Rossa and M. Tavakoli, "Issues in closed-loop needle steering," *Control Engineering Practice*, vol. 62, pp. 55–69, 2017.

[23] M. P. Ottensmeyer and J. K. Salisbury, *In Vivo Data Acquisition Instrument for Solid Organ Mechanical Property Measurement*. Berlin, Heidelberg: Springer Berlin Heidelberg, 2001, pp. 975–982.

[24] Min-Hua Lu, W. Yu, Qing-Hua Huang, Yan-Ping Huang, and Yong-Ping Zheng, "A Hand-Held Indentation System for the Assessment of Mechanical Properties of Soft Tissues In Vivo," *IEEE Transactions on Instrumentation and Measurement*, vol. 58, no. 9, pp. 3079–3085, sep 2009.

[25] D. Fu, S. F. Levinson, S. M. Gracewski, and K. J. Parker, "Non-invasive quantitative reconstruction of tissue elasticity using an iterative forward approach," *Physics in Medicine and Biology*, vol. 45, no. 6, pp. 1495–1509, 2000.

[26] K. Nightingale, S. McAleavey, and G. Trahey, "Shear-wave generation using acoustic radiation force: in vivo and ex vivo results," *Ultrasound in Medicine & Biology*, vol. 29, no. 12, pp. 1715–1723, 2003.

[27] J. Reddy, *An Introduction to the Finite Element Method*, 2nd ed., ser. McGraw-Hill series in mechanical engineering. McGraw-Hill, 1993.

[28] J. Carriere, C. Rossa, R. Sloboda, N. Usmani, and M. Tavakoli, "Real-time needle shape prediction in soft-tissue based on image segmentation and particle filtering," in *2016 IEEE International Conference on Advanced Intelligent Mechatronics (AIM)*. IEEE, July 2016, pp. 1204–1209.